RESEARCH ARTICLE

NANO · MICRO small
www.small-journal.com

High-Stability Ionic Conductive Filtering Transistors for Bio-Inspired Signal Processing

Wanrong Liu, Jingwen Wang, Pengshan Xie, Xiangxiang Feng, Yunchao Xu, Chenxing Jin, Xiaofang Shi, Ruihan Li, Johnny C. Ho, Junliang Yang,* and Jia Sun**

Applying low-pass filters in satellite communications effectively eliminates unwanted high-frequency signals and noise during image capture, mirroring the human brain's selective filtering of sensory stimuli. To enhance the efficiency of signal processing for remote sensing images, a neuromorphic information processing array based on oxide field-effect transistors are developed with HfO_2-lithium aluminium germanium phosphate (LAGP)-HfO_2 stacked dielectric (HLH FETs). The Li-ion solid-state electrolytes are stabilized in complex environments (extreme temperature and magnetic field) due to the protective sandwich structure. Meanwhile, the excellent insulating properties and Li-ion isolation effect of the high-k dielectric layer ensure a long-term reliable neuromorphic response for low-pass filtering (over one year in air). Hardware modules derived from HLH FETs are not only applicable to image processing but also show promising potential in edge computing and artificial intelligence, facilitating pattern recognition and noise reduction through biomimetic low-pass filtering functions. This innovative approach offers a new solution for modern satellite remote sensing technology and signal processing.

1. Introduction

As satellite orbits become increasingly congested, traditional data processing and transmission systems are facing significant challenges.[1,2] The exponential growth of remote sensing, earth observation, and communication applications has generated an unprecedented volume of raw data, leading to high energy demands for transmission.[3] This strain is further compounded by the limitations of current satellite architectures, which often relay vast amounts of unprocessed data back to ground stations.[4] Conventional on-orbit processing modules,[5] which could alleviate this burden, typically involve intricate circuit architectures and complex system designs.[6,7] These systems must meet the computational requirements for real-time data analysis while ensuring compatibility with space-grade components. The inherent constraints of weight, power consumption, and thermal management further complicate their design. Moreover, the extreme conditions of space, including temperature fluctuations, impose stringent demands on the reliability and stability of every device. From the rigorous launch phase to extended operational lifespans, each unit must demonstrate exceptional durability and consistent performance.

To tackle these challenges, there is a growing focus on developing innovative solutions that combine durable materials, efficient processing, and lightweight designs. Neuromorphic devices are emerging as a promising approach for edge computing applications in this context.[8–10] These devices offer significant advantages due to their low energy consumption, real-time data processing, and adaptability. By emulating the neural behaviors of the human brain, neuromorphic devices efficiently filter out redundant information and retain only critical data with minimal energy consumption,[11–14] which is particularly important in satellite communications. The parallel computing capabilities of neuromorphic devices enable satellites to analyze and process data in real time, reducing dependency on ground stations and minimizing data transmission delays. Furthermore, their adaptability allows them to adjust strategies based on environmental changes, enhancing the system's flexibility and intelligence. Their high fault tolerance and edge computing capabilities ensure greater reliability and efficiency for satellite systems in extreme space environments.

W. Liu, J. Wang, X. Feng, Y. Xu, C. Jin, X. Shi, R. Li, J. Yang, J. Sun
Hunan Key Laboratory for Super Microstructure and Ultrafast Process
School of Physics
Central South University
Changsha, Hunan 410083, P. R. China
E-mail: junliang.yang@csu.edu.cn; jiasun@csu.edu.cn

P. Xie, J. C. Ho
Department of Materials Science and Engineering
City University of Hong Kong
Kowloon, Hong Kong 999077, P. R. China
E-mail: johnnyho@cityu.edu.hk

W. Liu, X. Feng, Y. Xu, C. Jin, X. Shi, R. Li, J. Yang, J. Sun
State Key Laboratory of Precision Manufacturing for Extreme Service Performance
College of Mechanical and Electrical Engineering
Central South University
Changsha, Hunan 410083, P. R. China

W. Liu, Y. Xu, C. Jin, X. Shi, R. Li, J. Sun
State Key Laboratory of Transducer Technology
Shanghai Institute of Microsystem and Information Technology
865 Changning Road, Shanghai 200050, P. R. China

J. Wang
School of Electronic Information
Central South University
Changsha, Hunan 410083, P. R. China

The ORCID identification number(s) for the author(s) of this article can be found under https://doi.org/10.1002/smll.202502874

DOI: 10.1002/smll.202502874

Solid-state electrolyte-based neuromorphic devices simulate the functions of biological neurons through ion migration and electrochemical reactions, demonstrating excellent plasticity and adaptive learning abilities with vast potential in intelligent computing and artificial intelligence.[15–17] Solid-state electrolytes offer huge advantages in terms of long-term device stability compared to liquid ionic electrolytes. Recent advances in materials science have empowered researchers to develop high-performance solid-state electrolytes, including inorganic,[18,19] polymer,[20–22] and composite electrolytes.[23–25] These solid-state electrolyte-based neuromorphic devices have broad application potential in smart devices, the Internet of Things (IoT), and edge computing, enabling real-time processing near data sources and reducing latency and bandwidth demands. However, improving device performance and system integration remains a key challenge in current research.

The multifunctionality of stacked dielectric materials presents broad application potential in information processing, energy storage, and signal transmission. Stacked dielectric structures provide optimized capacitance, enhanced insulation, and higher dielectric strength,[26–28] which are effective ways to improve the electrical performance and stability of solid-state electrolyte transistors. High-k dielectrics, with their high dielectric constant, demonstrate excellent stability under high-temperature and high-frequency conditions,[29–31] ensuring device reliability in demanding environments. Stacking solid-state electrolytes with high-k oxide dielectrics offers advantages in performance, reliability, and integration, positioning these technologies as key components in next-generation electronic devices and providing strong support for future innovations in intelligent technology.

In this work, we proposed a neuromorphic information processing array with In_2O_3 field-effect transistors by employing HfO_2-LAGP-HfO_2 stacked dielectric as a gate insulator, known as HLH FETs. These devices demonstrate inherent low-pass filtering characteristics and excellent electrical stability (over one year in air condition). The HLH stacked dielectric films offer superior insulation and electrical properties, maintaining outstanding performance even in high-temperature environments (500 K) and strong magnetic field environment (1.5 T). Theoretical analysis revealed that HfO_2 dielectric films can mitigate adverse Li ion doping, thereby ensuring the long-term stability of the device. Furthermore, the low-pass filtering capabilities of HLH FETs are not only applicable to image processing but also hold promising prospects in edge computing and artificial intelligence. These devices facilitate pattern recognition and noise reduction by leveraging biomimetic low-pass filtering functions, indicating a wide range of potential applications. This innovative approach provides a novel solution for modern satellite communications technology and signal processing.

2. Results

2.1. Low-Pass Filter Applied to Satellite Communications

In earth observation satellites, low-pass filters are commonly utilized for image and video signal processing to eliminate unnecessary signals, thereby reducing high-frequency noise in the captured images. Traditional remote sensing imaging satellite systems acquire image data in orbit, then downlinked for processing and distribution by ground processing centers (**Figure 1**ai). However, as the volume of satellite data rapidly increases, the gap between the massive amounts of data generated and the limitations of satellite-to-ground digital transmission has become increasingly apparent. Moreover, the conventional satellite application process is complex and cumbersome, making it difficult to meet the high time-sensitivity requirements of various missions. Consequently, on-orbit processing of high-resolution remote sensing images is an effective solution to these challenges. The human brain receives vast amounts of information daily, including inputs from visual,[32–34] auditory,[35] tactile,[36,37] and olfactory sensory organs.[38–40] It can quickly store and process information, filtering out irrelevant data to reduce cognitive load. This filtering function allows us to selectively focus on and process the most relevant information amidst many environmental stimuli, enabling rapid feature processing and recognition while ignoring unnecessary details or distractions (Figure 1aii). To address these challenges, we propose the development of a single-processing hardware module for low-pass filtering designed to withstand extreme environments. This device leverages its inherent low-pass filtering capabilities and stable operational advantages to perform real-time preprocessing of large volumes of raw data directly on the satellite in orbit. The processed, lightweight data is then downlinked to ground processing centers for broader applications. This approach helps significantly reduce transmission costs while also extending the satellite lifespan.

To emulate the brain's ability to filter complex information, we have designed a FET featuring heavily-doped n-type silicon (n-Si)/ HLH stacked dielectric/In_2O_3 semiconductor/Al source-drain electrodes, which can be applied in single-processing hardware modules for low-pass filters (Figure 1b). The detailed fabrication methods are described in the Methods section. The stacked HLH sandwich structure typically exhibits optimized capacitance, improved insulation properties, and higher dielectric strength, concurrently enhancing the electrical characteristics and stability of the device. To further illustrate the structure of the stacked dielectric films, we characterized the cross-section of the dielectric layer using high-resolution transmission electron microscopy (TEM) (Figure 1c). The HLH stacked dielectric films were observed to have clear interfaces, indicating that the prepared dielectric films are uniform, with thicknesses measured from bottom to top as 8.7 nm, 36 nm, and 7.4 nm, respectively (Figure S1, Supporting Information). Energy-dispersive X-ray spectroscopy (EDS) mapping of the cross-section of the dielectric films also indicated a homogeneous axial and radial distribution of Hf and Ge elements (Figure 1d; Figure S1b, Supporting Information). Interestingly, the HfO_2 dielectric film, grown through magnetron radio-frequency (RF) sputtering at room temperature, revealed lattice fringes with interplanar spacings of approximately 2.96 Å (Figure 1c), similar to the (111) interplanar spacing of the monoclinic HfO_2 phase reported in the literature.[26,41] The X-ray diffraction (XRD) of the HfO_2 film further confirms the presence of a crystalline peak on the (111) plane (Figure S2, Supporting Information). Furthermore, the 2D grazing incidence wide-angle X-ray scattering (GIWAXS) diffraction pattern of the HLH stacked dielectric films displayed complete polycrystalline rings with (111) orientation, consistent with TEM and XRD results (Figure 1c). The peak information for in-plane and

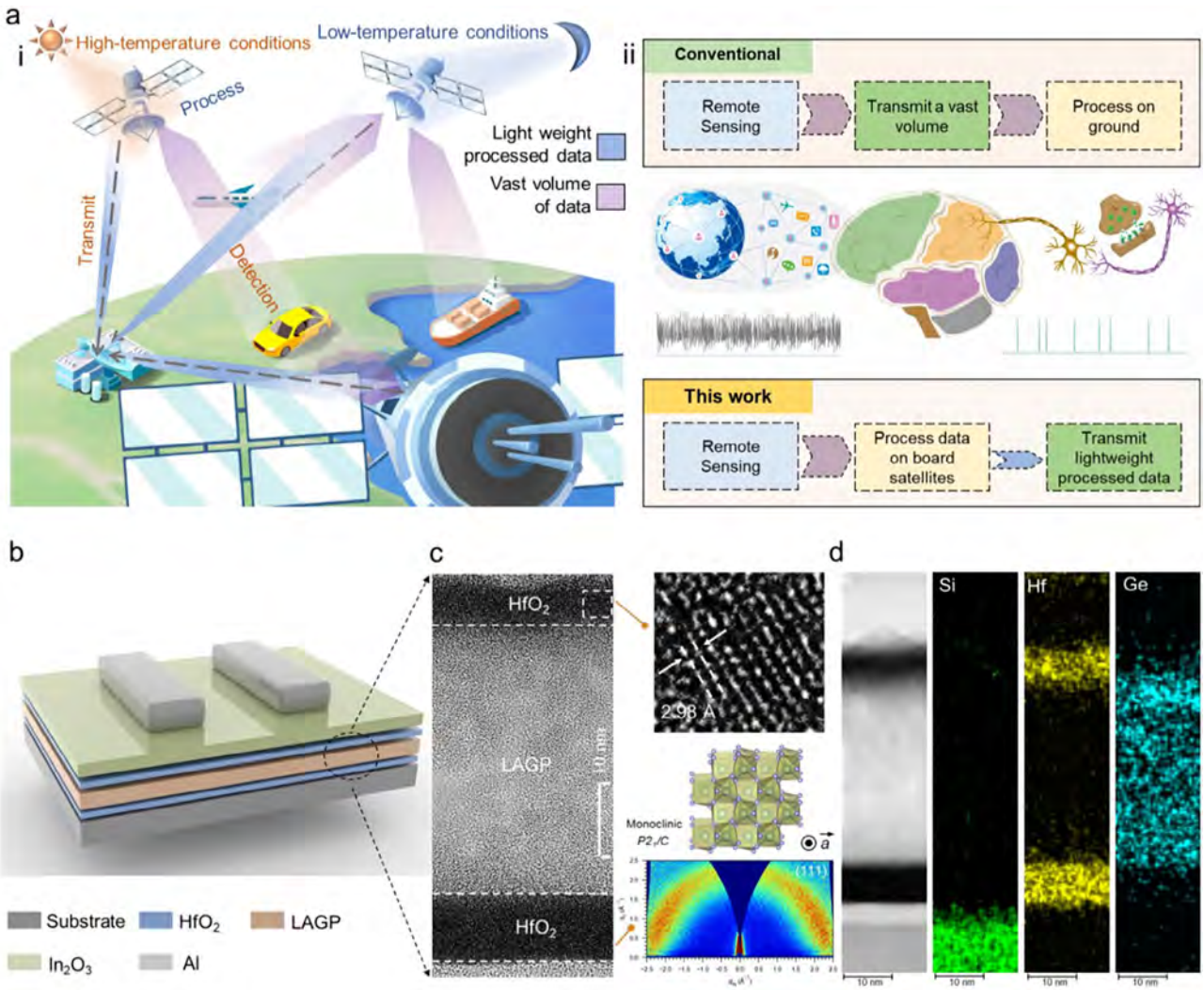

Figure 1. Remote Sensing Satellite Imaging and Device Structure Representation. a) Traditional remote sensing satellite imaging and innovative remote sensing satellite imaging process based on filtered neuromorphic devices. b) Schematic diagram of the transistor structure with an HfO_2/LAGP/HfO_2 layered dielectric layer. c) Cross-sectional TEM image of the HfO_2/LAGP/HfO_2 layered dielectric film, the right are the enlarged images of the HfO_2 crystalline region, the schematic diagram of the crystal structure, and the grazing incidence 2D GIWAXS characterization of the HLH stacked dielectric. d) Cross-sectional energy-EDS of the HfO_2/LAGP/HfO_2 layered dielectric film, displaying Si, Hf, and Ge elements.

out-of-plane were shown in Figure S3 (Supporting Information). By etching with X-ray photoelectron spectroscopy (XPS) at different times, the elements of different functional layers were gradually exposed and disappeared, demonstrating the sandwich structure and tunability of the HLH functional stacking layer (Figure S4, Supporting Information).

2.2. Electrical Performance Characterization of Devices

The neuromorphic behavior of transistors based on solid-state Li-ion electrolytes in biological neural networks has widespread applications in neuromorphic computing and artificial intelligence. The Li ions moving within the solid-state electrolytes can effectively regulate the semiconductor channel. When Li ions migrate to the semiconductor interface, they alter the charge density of the channel, thereby affecting its conductive state. This process is analogous to the transmission of chemical neurotransmitters in biological neurons. However, overly active Li ions tend to cause uncontrollable insertion/extraction at the semiconductor-dielectric interface, a key factor leading to device instability. Improvements can be made through material selection, interface engineering, and structural design to ensure that Li-ion devices maintain excellent performance under long-term and multiple-cycle conditions. Therefore, we explored the performance of HLH sandwich-structured dielectric films with varying thicknesses and the effect of introducing HfO_2 dielectric layers on device stability. In order to ensure the repeatability and consistency of the devices, the HfO_2 films in the HLH stacked dielectric layers were prepared under identical conditions and had the same thickness (the specific thickness of each layer is shown in Figure S5, Supporting Information). Surface morphology analysis was

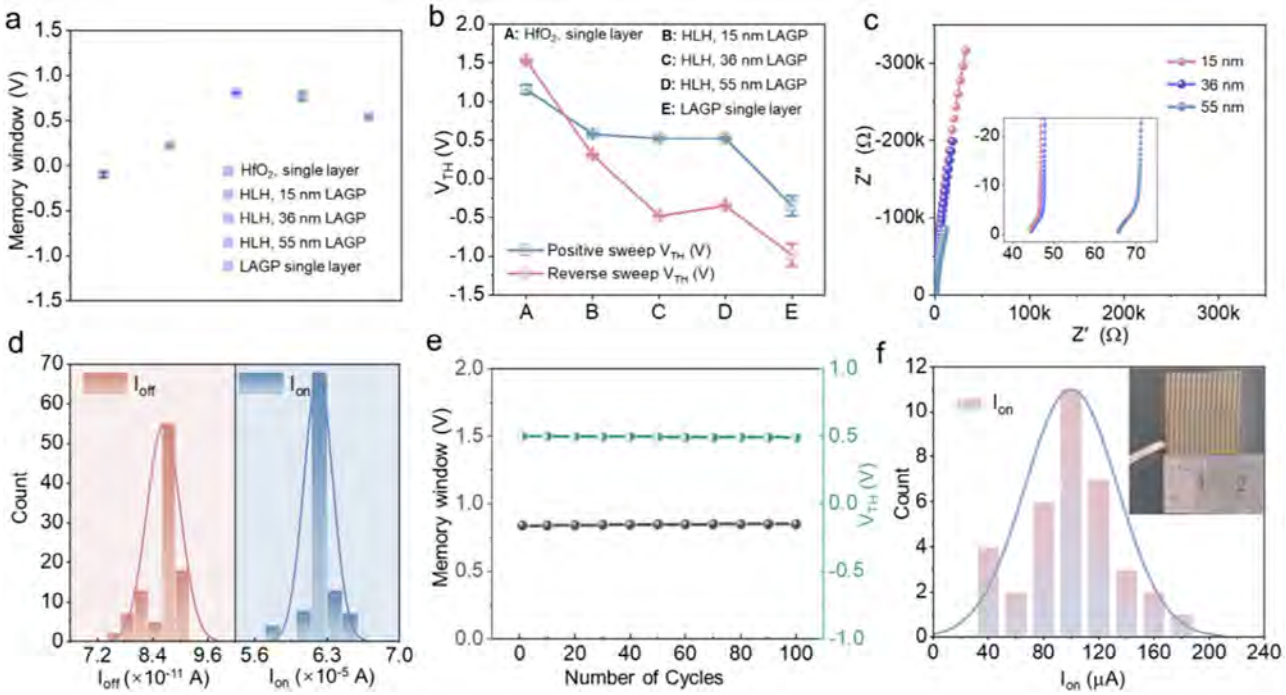

Figure 2. Electrical Characteristics of In_2O_3 Transistors Based on Single-Layer HfO_2, LAGP Dielectric Films, and HfO_2/LAGP/HfO_2 Layered Dielectric Films. a) Variation in hysteresis window of In_2O_3 transistors with single-layer and layered dielectric films. b) Threshold voltage variation of In_2O_3 transistors with single-layer and layered dielectric films, with the blue line representing the threshold voltage during forward scanning and the orange line during reverse scanning. c) Nyquist plot of LAGP dielectric layers with different thicknesses. d) Normal distribution of the on/off state currents from 100 device transfer curve testing cycles. e) Statistical changes in memory window and forward threshold voltage from 100 device transfer curve testing cycles. f) Normal distribution statistics of the ON-state current in a 6×6 device array.

conducted on single-layer and stacked dielectric films of different thicknesses using atomic force microscopy (AFM) (Figure S6, Supporting Information). The root-mean-square (RMS) surface roughness of the single-layer hafnium oxide film was 0.358 nm, indicating a very uniform and dense hafnium oxide deposited via magnetron sputtering. A certain thickness is necessary to ensure the working efficiency of the solid-state electrolyte. However, the thicker the electrolyte film was, the higher the roughness raised. The optimized single-layer LAGP dielectric film had an RMS surface roughness of 1.319 nm. This may hinder the subsequent deposition of In_2O_3 semiconductor films and can result in poor interface contact between the semiconductor and dielectric layer, adversely affecting device stability. Introducing the top HfO_2 dielectric layer could significantly reduce the surface roughness, ensuring stable operation of arrays with large inorganic channels. Figure S7 (Supporting Information) presents the transfer characteristic curves of In_2O_3 transistors with single-layer HfO_2, LAGP, and HLH stacked dielectric films, respectively. A counterclockwise hysteresis window is observed in the transfer curves of In_2O_3 devices with single-layer LAGP and HLH stacked dielectric films, primarily due to the formation of a double electric layer as Li ions move under an external field.[15,16,42] Correspondingly, the only monoclinic polycrystalline HfO_2 layer demonstrates typical properties of high-k insulating layers with a small clockwise hysteresis window, possibly due to negligible oxygen vacancies in HfO_2 and surface trap states. In HLH devices, increasing the LAGP thickness enlarges the counterclockwise hysteresis window until saturation (**Figure 2a**), showing the modulation of channel carrier lifetime by different Li-ion concentrations. In general, the operational stability and leakage current of solid-state electrolyte-based FET devices are problems that need to be overcome because of ionic penetration and surface defects. Here, single-layer LAGP dielectric film devices also suffered from detrimental drift after multiple scans (Figure S7e, Supporting Information), likely due to high interfacial roughness hindering In_2O_3 semiconductor film formation, resulting in poor interface contact between the dielectric layer and semiconductor and irreversible Li ion doping under an external field. Figure 2b summarizes the threshold voltages (V_{TH}) during forward and reverse scans of these devices. The device V_{TH} shifts positively with the addition of HfO_2, allowing control over device V_{TH} by adjusting the thickness of the LAGP film in the stacked dielectric layer. The sandwich structure effectively increased the storage window of the devices and controlled the turn-on voltage in a smaller range, reducing the power consumption. The error bars also demonstrate minimal V_{TH} drift in HLH sandwich dielectric film transistors, indicating good device stability. Furthermore, the breakdown resistance of single-layer LAGP films and HLH stacked dielectric films were studied (Figure S8, Supporting Information). From the ten randomly tested capacitor devices, it can be seen that the breakdown field strength of the single-layer LAGP dielectric varies from 1.12 to 8.47 MV/cm, while the HLH stacked dielectric films fluctuate between 8.17 and 9.42 MV/cm. The sandwich-structured films exhibit a more stable breakdown resistance. As seen in Figure S9a (Supporting Information), the gate leakage current of stacked

dielectric layer transistors is in the nA range, ensuring device reliability and stability and meeting the requirements for advanced transistors regarding gate leakage current. Output characteristic curves in Figure S9b (Supporting Information) reveal that the Al electrode forms a good Ohmic contact with the semiconductor. The electrical performance of devices based on the HLH sandwich dielectric layer demonstrates the ability of the devices to realize neuromorphic response under low energy supply environments, which satisfies the requirements for integration in remote sensing communication devices such as solar-powered satellites.

To further understand the working mechanism of LAGP, we tested the capacitance-frequency relationship of three stacked dielectric films (Figure S10, Supporting Information). As thickness increases, capacitance decreases, and greater LAGP thickness results in decreased capacitance at high frequencies, akin to ion-regulated dielectrics. Figure 2c displays Nyquist plots for LAGP ionic dielectric films of various thicknesses (15 nm, 36 nm, 55 nm), where the high-frequency semicircular region corresponds to electron transport limitations, and the low-frequency linear region corresponds to diffusion limitations.[43,44] The slope in the low-frequency region indicates that thicker LAGP ionic dielectric films have higher ionic conductivity; overly active Li ions may lead to unstable doping, reducing device stability. The HLH transistor with a 36 nm thick LAGP exhibits the most stable performance, as shown in Figure S11 (Supporting Information), where the transfer characteristic curves of the most stable stacked dielectric film transistor remain virtually unchanged after 100 cycles. Figure 2d shows the normal distribution of the on/off-state current (I_{on}/I_{off}) in the device after 100 cycles, with off-state currents ranging from 7.4 to 9.2 ($\times 10^{-11}$A), centering around 8.6 ($\times 10^{-11}$A), and on-state currents ranging from 5.6 to 6.6 ($\times 10^{-5}$ A), centering around 6.1 ($\times 10^{-5}$ A). Figure 2e presents the variations in hysteresis window and V_{TH} over 100 cycles, with the hysteresis window consistently at 0.85 V and the V_{TH} at 0.5 V, showing favorable anti-fatigue properties. Moreover, owing to the uniform preparation of large areas of the magnetron sputtering process, a 2.2 cm HLH FETs array (inset in Figure 2f) was fabricated. We selected one of the 6 × 6 arrays for consistency testing (Figure S12, Supporting Information), where the on-current follows a normal distribution centered around 100 μA. After one year of exposure to air, the HLH FET devices maintain a substantial on-current, demonstrating superior stability to devices using ion gels (Figure S13, Supporting Information).

2.3. Device Stability and Mechanism Analysis

The stability of devices in extremely complex environments is also a critical concern. The Curie temperature of ferroelectric functional layers and ferroelectric 2D semiconductors, currently widely used in neuromorphic devices, is generally low. In an environment above 450 K, the thin-film and low-dimensional functional layers are difficult to continue to work, and even only room temperature ferroelectricity can be realized.[45–47] For ion-gate devices, those with ionic liquid gates and polymer gate dielectrics change ionic conductivity due to moisture evaporation at high temperatures over time, subsequently affecting device performance.[48] Additionally, the dielectric is prone to breakdown at elevated temperatures, leading to increased gate leakage currents. In order to meet the demands of working in complex environments, the HLH FETs demonstrate favorable performance even under high-temperature peaks of 500 K (**Figure 3a**). As the temperature increases from room temperature to 500 K, the peak transconductance (g_m) gradually rises, and the V_{TH} shifts progressively to the left (Figure 3b), attributed to enhanced ion activity at elevated temperatures. This causes more Li ions to migrate to the HfO_2-LAGP interface, resulting in greater channel conductance regulation. In this case, HfO_2 prevents high-temperature active Li ions from affecting the semiconductor channel and provides effective insulating properties. Furthermore, the HLH FETs demonstrate gate voltage-tunable channel conductance behavior at low temperatures (Figure S14a, Supporting Information). As the temperature decreases, the V_{TH} shifts to the left and the g_m peak decreases (Figure S14b, Supporting Information). This is primarily due to restricted ion activity at low temperatures. The In_2O_3 transistors based on HLH stacked dielectrics exhibit excellent temperature tolerance and can operate over a wide temperature range from 10K to 500K. Moreover, the device remained stable when a magnetic field of varying strength was applied perpendicular to the direction of the channel, showing the potential for long-term operation in strong magnetic field environments (Figure S15, Supporting Information). This characteristic presents potential applications in space remote sensing signal processing. Figure 3c illustrates endurance testing under pulse sequence write and erase operations. The pulse amplitude and width are set for write voltage V_P (2 V, 100 ms) and erase voltage V_E (-2 V, 100 ms), respectively. Under the stimulus of applied positive/negative gate voltage, the formation/depletion of channel electrons is modulated, triggering changes in channel conductance. Moreover, after 10000 switching cycles, the device shows almost no degradation in performance, demonstrating exceptional operational stability. To further explore the mechanisms underpinning the enhancement in device stability, density functional theory (DFT) calculations were conducted. Given the small ionic radius of Li ions, they can efficiently adsorb at interstitial sites within the In_2O_3 and HfO_2 lattices. As shown in Figure 3d, the calculated adsorption energy results indicate that Li ions possess higher adsorption energy of -2.58 eV at interstitial sites in the In_2O_3 lattice. In contrast, they exhibit a lower adsorption energy of -0.39 eV in the HfO_2 lattice. This explains why In_2O_3 materials easily capture free Li ions, thus compromising device stability. Conversely, HfO_2 has a weaker capacity to capture Li ions, helping isolate Li ions' influence on the channel, thus enhancing device stability. Based on the theoretical calculation results, schematic diagrams illustrating the operating principles of single-layer LAGP dielectric film transistors and stacked dielectric film transistors were constructed (Figure 3d), showing ion migration under positive gate bias. Due to the small size of Li ions, they migrate in the direction of the electric field lines under an applied positive voltage. In single-layer LAGP dielectric film transistors, Li ions move to the In_2O_3 semiconductor interface or within In_2O_3. Given the high adsorption energy at the interstitial sites in the In_2O_3 lattice, they struggle to return to their original positions, and uncontrolled ion doping undermines long-term device stability. In contrast, in stacked dielectric film transistors, the lower HfO_2 dielectric film provides excellent electrical insulation, preventing leakage current, while the upper HfO_2 dielectric

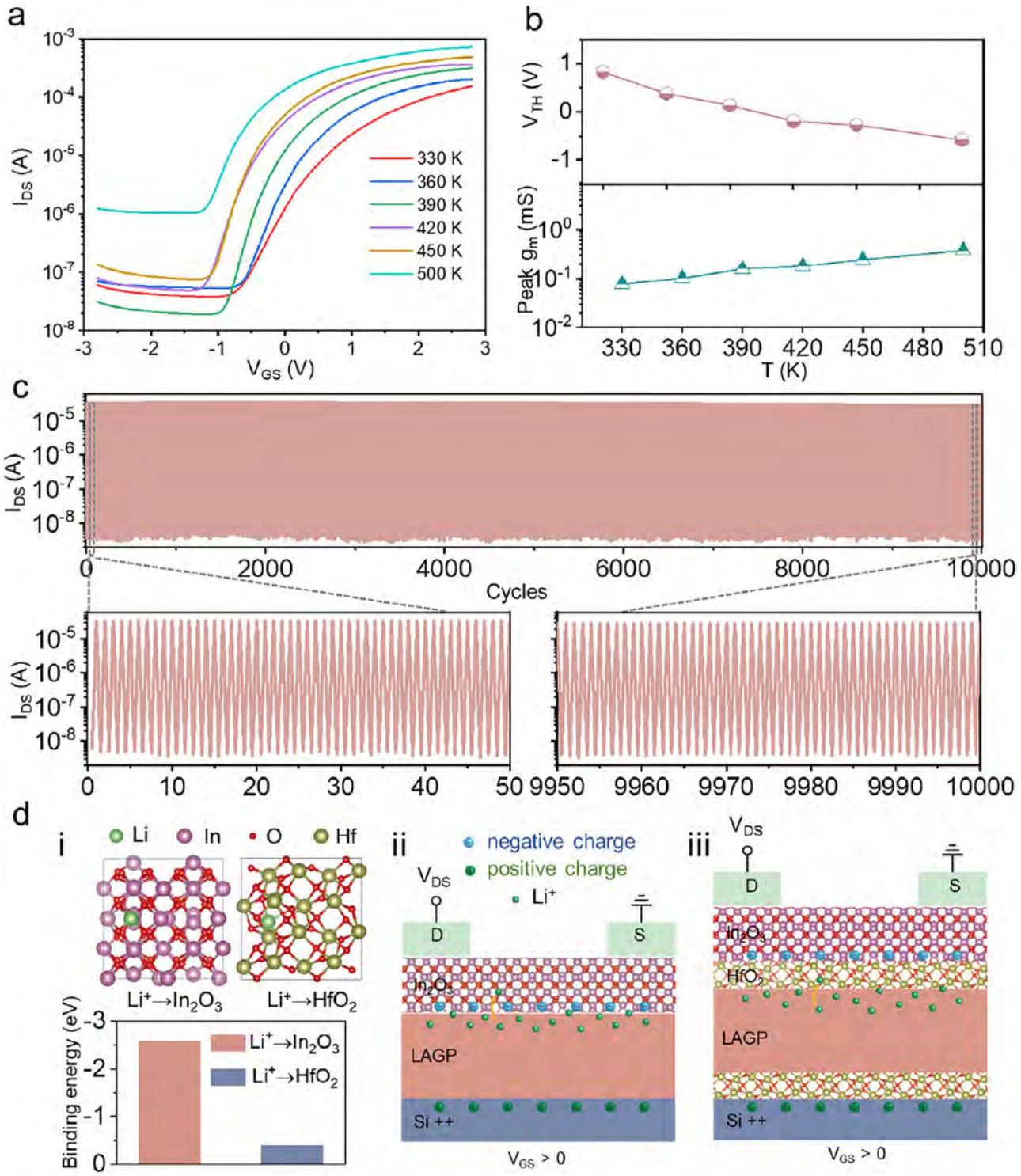

Figure 3. Electrical Stability and Stability Mechanism Analysis of In_2O_3 Transistors with Layered Dielectric Films. a) Transfer characteristic curve of HLH FETs device at high temperature. b) The V_{TH} value and peak g_m value as a function of the operating temperature. c) Endurance of In_2O_3 transistors, exceeding 1000 on/off cycles, with $V_P = 2$ V and $V_E = -2$ V. d) The Left panel shows the adsorption energy of Li ions on In_2O_3 and HfO_2 layers obtained through first-principles calculations, which are -2.58 eV and -0.39 eV, respectively. The middle and right panels depict the schematic ion migration of Li ions in the In_2O_3 film and HfO_2 film, respectively.

film improves growth conditions for the semiconductor film and blocks adverse Li ion doping. Under an applied gate voltage, Li ions migrate upwards along the electric field lines, accumulating at the upper HfO_2/LAGP interface or migrating into the HfO_2 interior. Given the weak adsorption capacity of HfO_2 (adsorption energy of -0.39 eV) for Li-ions, they can return to their original positions upon applying an erase voltage. Consequently, the proposed oxide transistors based on stacked dielectric films exhibit reliability and durability.

2.4. Hardware Signal Processing Based on Low-Pass Filtering Characteristics

In modern satellite remote sensing technology, managing signal and noise from detectors is one of the core challenges. Given that the human brain cannot perceive high-frequency stimuli in external signals, it implies that the brain functions as a low-pass filter for rapidly changing external inputs. For instance, the human eye cannot detect high-frequency flickers in fluctuating light signals due to visual persistence. Inspired by this, we explore the application of HLH FET devices in edge computing to develop a method for faster data analysis and real-time noise reduction, thereby enhancing the accuracy and reliability of remote sensing data. This approach utilizes the low-pass filtering characteristics of HLH FET devices to implement a multimodal biomimetic method, which achieves high-frequency noise removal to further conduct pattern recognition tasks for better results. To be specific, in the process of remote sensing, each device is responsible for one of the n observation pixels and processes their temporal incoherent fluctuations, which correspond to noise. The devices first filter these noise-containing signals in parallel, and the filtered data is subsequently reconstructed to ultimately obtain clear image information, as illustrated in **Figure** 4a. This concept integrates the advantages of pre-processing and analyzing image and audio data, employing low-pass filtering techniques to minimize noise during data processing and providing more possibilities for hardware deep learning neural network models to improve image recognition accuracy further.

To verify the low-pass filtering characteristics of the HLH FETs device, we conducted an MSO_5 task. The MSO_5 task consists of 1000-time steps (Figure S16, Supporting Information). The generated time series, u(t) and -u(t), were linearly mapped to an appropriate voltage range (-2 V, 2 V), with a time interval of 20 ms between each time step. The input was then applied to the HLH FETs device, which has a thickness of 52 nm, where the thickness of the LAGP is 36 nm, and 1000 stability tests were conducted. Specifically, each input consists of 1000-time steps, with each group cycle containing 50 inputs, repeated 20 times. We present the dynamic current response of the 3 group cycles: the 1st group cycle, the first cycle of the 1st group cycle, the 10th and 20th group cycles, and the final cycle of the 20th group cycle, as shown in Figure 4b. The dynamic current responses and Fast Fourier Transform (FFT) analyses for different thicknesses and materials are provided in Figure S17 (Supporting Information). FFT was performed on the MSO_5 input and the device's current responses, with five peaks corresponding to five distinct frequencies. Figure 4bi displays the FFT of the 1st cycle output, while Figure 4bii displays the FFT of the original MSO_5 input. Figure 4biii presents the FFT of the entire 20th group cycle, and Figure 4biv depicts the FFT of the final cycle output after the 20th group cycle. These results indicate that devices with an HLH thickness of 52 nm can not only effectively suppress high-frequency components but also maintain excellent stability even after 1000 repeated operational cycles. Furthermore, the dynamic current response and FFT analysis of the HLH device under the MSO_5 task input after being stored in ambient air for one and a half years are shown in Figure S18 (Supporting Information). These results indicate that the device retains excellent high-frequency signal suppression capabilities even after prolonged ambient exposure.

As a proof of concept, we utilized a single device to process each pixel in the image for image filtering. To demonstrate its low-pass filtering and denoising capabilities, we processed the images of "C", "S", and "U", showcasing the results with detailed image processing steps provided in Figure S19 (Supporting Information). The pixel grayscale values were mapped to various voltage ranges and tested with different input frequencies for comparative analysis. By adjusting the time interval between these points in the same input voltage list on our testing platform, we manually generate input signals of varying frequencies-shorter intervals correspond to higher input frequencies, and longer intervals to lower ones. As illustrated in Figure 4c, at a frequency of 50 Hz and a voltage range of (-2 V, 2 V), information can be effectively distinguished from noise, with primary information enhanced and background noise suppressed, resulting in a clear contrast. Display results for other settings are presented in Figure S20 (Supporting Information). However, the effect may become less noticeable or indiscernible if the input frequency is excessively high or the voltage range mapping is too narrow. This also indicates that the processing results of the device can be optimized by adjusting the input frequency and the mapping range of the voltage. These findings suggest that the HLH FETs device can simplify hardware circuits and enhance functionality in neuromorphic applications.

To further illustrate this, the processing results under different input conditions are compared. When the input conditions are set to (50 Hz, (-1 V, 1 V)), the output current cannot effectively differentiate between information and noise. As a result, the noise distribution in the original image closely mirrors that in the after output, indicating minimal improvement. This is evident in Figure 4di, where the results processed by HLH FET (HLH /8.7-36-7.4 nm) reveal a lack of filtering. In contrast, by maintaining the input frequency and adjusting the voltage mapping range, the Figure 4dii highlights the enhanced filtering capability of HLH FET (HLH /8.7-36-7.4 nm). Under these conditions, most noise in the output current is nearly eliminated, creating a distinct contrast with the primary information. The complete output current-frequency bar chart showcasing the primary information is provided in Figure S21 (Supporting Information). Comparing with traditional digital filtering techniques, our device does not exhibit a sharp step-function-like cutoff, instead, the smooth transition in our device avoids Gibbs-induced ringing, preserves critical details near the cutoff, and enables natural denoising without distorting mixed-frequency signals. Further, conventional transistor sensors typically rely on intricate algorithms to achieve complex functions. However, as algorithmic development approaches inherent limitations, high-performance

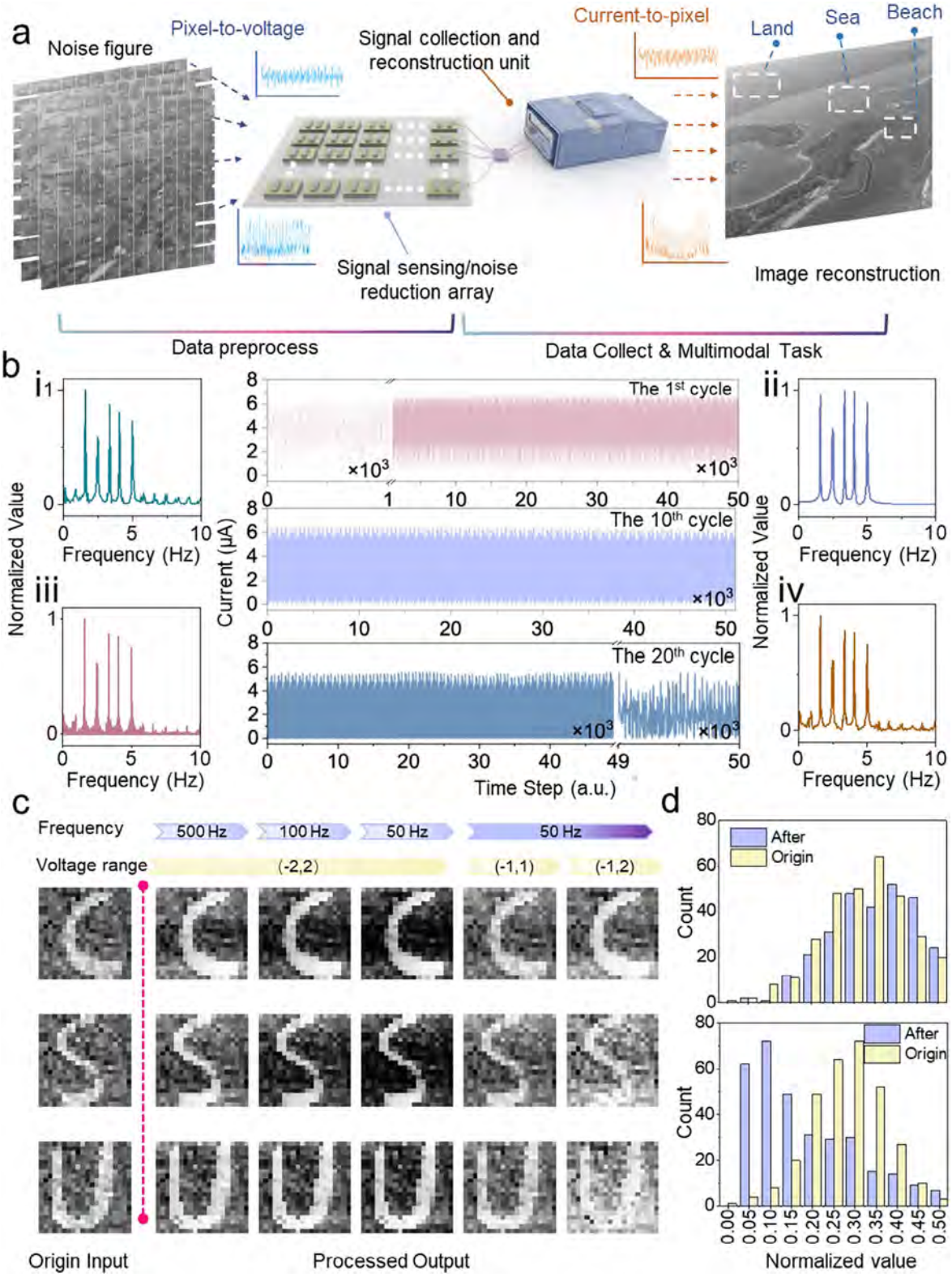

Figure 4. Hardware Image Processing based on Low-Pass Filtering Characteristics. a) Illustration of integrating a hardware image processing unit with the central processing unit, which improves recognition task efficiency by offloading image processing from the central unit. b) 1000 stability test cycles output of the MSO_5 task input and FFT analysis of (i) output from the first cycle, (ii) original input signal, (iii) total output from the 20th set of 50 cycles, and (iv) output from the final cycle, respectively. c) The denoising results under different combinations of input frequency and voltage range. d) The noise bars before and after denoising processing for two different test conditions.

transistors with specialized capabilities present a new frontier. By leveraging bio-inspired transistors designed for AI, these devices can operate effectively with simplified algorithms, paving the way for streamlined, high-efficiency applications. We expect to unlock even greater complexity and application potential by integrating biomimetic, low-pass filtering technologies and multimodal AI. Future efforts will focus on refining these integrations to optimize performance and support the practical demands of edge computing or advanced AI systems.

3. Conclusion

This work focuses on developing In_2O_3 FETs with HLH stacked dielectric, which demonstrate inherent low-pass filtering characteristics and excellent electrical stability, especially in wide-range-temperature environments. The HLH stacked dielectric films provide superior insulation, mitigating improper Li-ion doping and enhancing device stability. These FETs are applicable in image processing, edge computing, and AI, utilizing biomimetic low-pass filtering to aid pattern recognition and noise reduction. This innovative approach offers new solutions for modern satellite communications and signal processing. Comprehensive characterization reveals that HLH FETs exhibit robust performance, even at high temperatures, due to their ability to modulate ionic movement, effectively mimicking the brain's selective filtering under complex conditions.

4. Experimental Section

Preparation of Samples: The heavily doped p-type silicon substrates were sequentially ultrasonically cleaned in ethanol, deionized water, and isopropanol for 20 min each at a power of 100 W. Subsequently, the substrates were baked in an oven set to 120 °C for 30 min. In the first step, dry Si substrates were placed on a magnetron sample holder, and a 7.6 nm HfO_2 dielectric film was grown on the substrate via RF magnetron sputtering. The chamber vacuum was maintained below 6×10^{-4} Pa before film deposition, with a sputtering pressure of 0.3 Pa, a sputtering power of 50 W, and a sample holder rotation speed of 20 rpm to ensure the deposition of a dense, high-quality HfO_2 dielectric film. Subsequently, LAGP dielectric films with thicknesses of 15 nm, 36 nm, and 55 nm were deposited using RF magnetron sputtering. This process involved introducing ultra-high purity argon and oxygen gases into the chamber at flow rates of 32 sccm and 8 sccm, respectively, under a sputtering pressure of 1 Pa and a power of 100 W, with the sample holder rotating at 20 rpm to obtain the LAGP dielectric film. Another dense, high-quality HfO_2 dielectric film was deposited under the same conditions, resulting in an HfO_2-LAGP-HfO_2 stacked dielectric film. In the second step, an In_2O_3 semiconductor film was deposited via RF magnetron sputtering, maintaining the chamber vacuum below 8×10^{-4} Pa. Ultrahigh purity argon and oxygen were introduced into the chamber at flow rates of 40 sccm and 4 sccm, respectively, with a sputtering pressure of 1 Pa, a power of 50 W, and a sample holder rotation speed of 20 rpm, yielding a 10 nm thick In_2O_3 semiconductor film. All dielectric and semiconductor films were deposited at room temperature without needing annealing. In the third step, a shadow mask technique was employed to thermally deposit 70 nm of aluminum for source and drain electrodes, maintaining a deposition rate of 3 ~ 5 Å/s with a channel width of 1000 µm and a length of 80 µm.

Measurements and Characterization: The electrical properties of the transistor devices were characterized using a standard probe station and a 4200 semiconductor parameter analyzer (Keithley 4200-SCS). TEM (Thermo Scientific, Talos F200X) and EDS was used to analyze the cross-sectional morphology and energy spectra of the dielectric layers. The crystalline structure of the dielectric layers was investigated using XRD (MiniFlex600, Rigaku) and 2D GIWAXS (Xenocs Xeuss 2.0). Elemental analysis of the stacked dielectric films was conducted using XPS (PHI VersaProbe 4, ULVAC-PHI), and AFM (5500 AFM, Agilent Technology) was used to analyze the surface morphology of the films.

Calculation of Binding Energy: The calculations were performed based on DFT using generalized gradient approximation of Perdew-Burke-Ernzerhof functional as implemented in the Vienna Ab initio Simulation Package.[49,50] The Valence-Core interactions were described by projector-augmented-wave pseudopotentials.[51] The cutoff energy of the plane wave was set to 500 eV. The calculations used a 2×2×2 Monkhorst-Pack k-point meshes to sample the Brillouin zone. All atoms were fully relaxed until the atomic Hellmann–Feynman forces were less than 0.02 eV $Å^{-1,}$ and the total energy change was less than 1×10^{-4} eV. The adsorption energy was calculated using the equation, $E = E_{A+B} - E_A - E_B$, where E_A was the energy of In_2O_3 or HfO_2 unit cell, E_B was the energy of isolated Li-ion, and E_{A+B} was the energy of the In_2O_3 or HfO_2 unit cell with an adsorbed Li-ion.

Ethical Statement: The author certifies that this manuscript was original and has not been published and will not be submitted elsewhere for publication while being considered by Advanced Materials. And the study was not split up into several parts to increase the quantity of submissions and submitted to various journals or to one journal over time. No data have been fabricated or manipulated (including images) to support your conclusions. No data, text, or theories by others were presented as if they were this own. The submission has been received explicitly from all co-authors. And authors whose names appear on the submission have contributed sufficiently to the scientific work and therefore share collective responsibility and accountability for the results.

Supporting Information

Supporting Information is available from the Wiley Online Library or from the author.

Acknowledgements

This study has been supported by the National Key Research and Development Program of China (No. 2023YFE0208600 and No. 2022YFB3803300), the National Natural Science Foundation of China (No. 62375288, No. U23A20138 and No. 52173192), the State Key Laboratory of Precision Manufacturing for Extreme Service Performance, Central South University (No. ZZYJKT2023-10), the Research Foundation of Education Bureau of Hunan Province (No. 23B0010), and Fundamental Research Funds for the Central Universities of Central South University (No.1053320215226).

Conflict of Interest

The authors declare no conflict of interest.

Author Contributions

W.L., J.W., and P.X. contributed equally to this work. W.L., J.W, and J.S. conceived the original concept and designed the experiments. W.L. fabricated the devices. W.L. and P.X. characterized the device's performance. W.J. and X.F. simulated and calculated the data. W.L., J.W., P.X., X.F., Y.X., C.J., X.S., R.L., J.C.H., J.Y., and J.S. contributed to analysis and discussion on the data. W.L. and W.J. wrote the manuscript with input from all the other authors. All authors discussed the results and commented on the manuscript.

Data Availability Statement

The data that support the findings of this study are available in the supplementary material of this article.

Keywords

low-pass filtering, neuromorphic computing, signal processing, stacked dielectric

Received: March 5, 2025
Revised: May 23, 2025
Published online:

[1] B. Zhang, Y. Wu, B. Zhao, J. Chanussot, D. Hong, J. Yao, L. Gao, *IEEE J. Sel. Top. Appl. Earth Obs. Remote Sens.* **2022**, *15*, 1814.
[2] T. Zhao, S. Wang, C. Ouyang, M. Chen, C. Liu, J. Zhang, L. Yu, F. Wang, Y. Xie, J. Li, *Innovation* **2024**, *5*, 100691.
[3] Y. Ma, H. Wu, L. Wang, B. Huang, R. Ranjan, A. Zomaya, W. Jie, *Future Gener. Comput. Syst.* **2015**, *51*, 47.
[4] Sisodiya, N., Nitant, D., Priyank, T., **2019**, In: *Hemanth, Remote Sensing and Digital Image Processing*, Springer, (Berlin), ISBN: p. 9783030241773.
[5] S. Wang, Q. Li, *IEEE Internet Things J.* **2023**, *10*, 22514.
[6] Y. Yang, K. Ren, J. Song, *Heliyon* **2024**, *10*, 32071.
[7] C. I. Nwakanma, J.-W. Kim, J.-M. Lee, D.-S. Kim, *ICT Express* **2021**, *7*, 152.
[8] Kamble, G. U., Patil, C. S., Alman, V. V., Kundale, S. S., Hyeok K., Neuromorphic Computing: Cutting-Edge Advances and Future Directions, Recent Advances in Neuromorphic Computing, IntechOpen, Croatia Zagreb **2024**.
[9] J. Minkiewicz, G. M. Jones, S. Ghanizadeh, S. Bostanchi, T. J. Wasely, S. A. Yamini, V. Nekouie, *Open Ceram* **2023**, *16*, 100497.
[10] H. Yang, K.-Y. Lam, L. Xiao, Z. Xiong, H. Hu, D. Niyato, H. Vincent Poor, *Nat. Commun.* **2022**, *13*, 4269.
[11] P. Li, M. Zhang, Q. Zhou, Q. Zhang, D. Xie, G. Li, Z. Liu, Z. Wang, E. Guo, M. He, C. Wang, L. Gu, G. Yang, K. Jin, C. Ge, *Nat. Commun.* **2024**, *15*, 3257.
[12] Q. Wang, C. Zhao, Y. Sun, R. Xu, C. Li, C. Wang, W. Liu, J. Gu, Y. Shi, L. Yang, X. Tu, H. Gao, Z. Wen, *Microsyst. Nanoeng.* **2023**, *9*, 96.
[13] C. Jiang, J. Liu, Y. Ni, S. Qu, L. Liu, Y. Li, L. Yang, W. Xu, *Nat. Commun.* **2023**, *14*, 1344.
[14] T. M. Hall, K. Nazarpour, A. Jackson, *Nat. Commun.* **2014**, *5*, 5462.
[15] D. Nishioka, T. Tsuchiya, W. Namiki, M. Takayanagi, M. Imura, Y. Koide, T. Higuchi, K. Terabe, *Sci. Adv.* **2022**, *8*, 1156.
[16] C. S. Yang, D. S. Shang, N. Liu, E. J. Fuller, S. Agrawal, A. A. Talin, Y. Q. Li, B. G. Shen, Y. Sun, *Adv. Funct. Mater.* **2018**, *28*, 1804170.
[17] S. Wang, X. Chen, C. Zhao, Y. Kong, B. Lin, Y. Wu, Z. Bi, Z. Xuan, T. Li, Y. Li, *Nat. Electron.* **2023**, *6*, 281.
[18] Q. Ma, H. Zhang, C. Zhou, L. Zheng, P. Cheng, J. Nie, W. Feng, Y. S. Hu, H. Li, X. Huang, L. Chen, M. Armand, Z. Zhou, *Angew. Chem., Int. Ed.* **2016**, *55*, 2521.
[19] Z. Zhang, Y. Shao, B. Lotsch, Y.-S. Hu, H. Li, J. Janek, L. F. Nazar, C.-W. Nan, J. Maier, M. Armand, L. Chen, *Energy Environ. Sci.* **2018**, *11*, 1945.
[20] P. M. Shanthi, P. J. Hanumantha, T. Albuquerque, B. Gattu, P. N. Kumta, *ACS Appl. Energy Mater.* **2018**, *1*, 483.
[21] A. Manthiram, X. Yu, S. Wang, *Nat. Rev. Mater.* **2017**, *2*, 16103.
[22] Y. Kim, A. Chortos, W. Xu, Y. Liu, J. Y. Oh, D. Son, J. Kang, A. M. Foudeh, C. Zhu, Y. Lee, S. Niu, J. Liu, R. Pfattner, Z. Bao, T.-W. Lee, *Science* **2018**, *360*, 998.
[23] W. Zhou, S. Wang, Y. Li, S. Xin, A. Manthiram, J. B. Goodenough, *J. Am. Chem. Soc.* **2016**, *138*, 9385.
[24] D. Lin, W. Liu, Y. Liu, H. R. Lee, P.-C. Hsu, K. Liu, Y. Cui, *Nano Lett.* **2015**, *16*, 459.
[25] Y. Van De Burgt, E. Lubberman, E. J. Fuller, S. T. Keene, G. C. Faria, S. Agarwal, M. J. Marinella, A. Alec Talin, A. Salleo, *Nat. Mater.* **2017**, *16*, 414.
[26] S. S. Cheema, N. Shanker, L.-C. Wang, C.-H. Hsu, S.-L. Hsu, Y.-H. Liao, M. San Jose, J. Gomez, W. Chakraborty, W. Li, J.-H. Bae, S. K. Volkman, D. Kwon, Y. Rho, G. Pinelli, R. Rastogi, D. Pipitone, C. Stull, M. Cook, B. Tyrrell, V. A. Stoica, Z. Zhang, J. W. Freeland, C. J. Tassone, A. Mehta, G. Saheli, D. Thompson, D. I. Suh, W.-T. Koo, K.-J. Nam, et al., *Nature* **2022**, *604*, 65.
[27] J. Choi, C. Lee, C. Lee, H. Park, S. M. Lee, C.-H. Kim, H. Yoo, S. G. Im, *Nat. Commun.* **2022**, *13*, 2305.
[28] J. Muller, T. S. Boscke, U. Schroder, S. Mueller, D. Brauhaus, U. Bottger, L. Frey, T. Mikolajick, *Nano Lett.* **2012**, *12*, 4318.
[29] S. K. Dubey, A. Islam, *Microsyst. Technol.* **2024**, *30*, 163.
[30] J. Singh, R. K. Chauhan, N. Yadava, *Adv. Theor. Simul.* **2024**, *7*, 2400365.
[31] J. Cui, F. An, J. Qian, Y. Wu, L. L. Sloan, S. Pidaparthy, J.-M. Zuo, Q. Cao, *Nat. Electron.* **2023**, *6*, 292.
[32] E. Baek, S. Song, C.-K. Baek, Z. Rong, L. Shi, C. V. Cannistraci, *Nat. Electron.* **2024**, *7*, 454.
[33] Y. Meng, F. Li, C. Lan, X. Bu, X. Kang, R. Wei, S. Yip, D. Li, F. Wang, T. Takahashi, T. Hosomi, K. Nagashima, T. Yanagida, J. C. Ho, *Sci. Adv.* **2020**, *6*, abc6389.
[34] J. Yu, X. Yang, G. Gao, Y. Xiong, Y. Wang, J. Han, Y. Chen, H. Zhang, Q. Sun, Z. L. Wang, *Sci. Adv.* **2021**, *7*, abd9117.
[35] S.-Y. Yun, J.-K. Han, S.-W. Lee, J.-M. Yu, S.-B. Jeon, Y.-K. Choi, *Nano Energy* **2023**, *109*, 108322.
[36] W. Wang, Y. Jiang, D. Zhong, Z. Zhang, S. Choudhury, J.-C. Lai, H. Gong, S. Niu, X. Yan, Y. Zheng, C.-C. Shih, R. Ning, Q. Lin, D. Li, Y.-H. Kim, J. Kim, Y.-X. Wang, C. Zhao, C. Xu, X. Ji, Y. Nishio, H. Lyu, J. B.-H. Tok, Z. Bao, *Science* **2023**, *380*, 735.
[37] S. Chen, Z. Zhou, K. Hou, X. Wu, Q. He, C. G. Tang, T. Li, X. Zhang, J. Jie, Z. Gao, N. Mathews, W. L. Leong, *Nat. Commun.* **2024**, *15*, 7056.
[38] J. K. Han, M. Kang, J. Jeong, I. Cho, J. M. Yu, K. J. Yoon, I. Park, Y. K. Choi, *Adv. Sci.* **2022**, *9*, 2106017.
[39] X. Wu, L. Jiang, H. Xu, B. Wang, L. Yang, X. Wang, L. Zheng, W. Xu, L. Qiu, *Adv. Funct. Mater.* **2024**, *34*, 2401965.
[40] H. W. Song, D. Moon, Y. Won, Y. K. Cha, J. Yoo, T. H. Park, J. H. Oh, *Sci. Adv.* **2024**, *10*, adl2882.
[41] Y. Ahn, Y. Jeon, S. Lim, J. Kim, J. Kim, H. Seo, *Surf. Interfaces* **2023**, *37*, 102669.
[42] Q. Wang, T. Zhao, C. Zhao, W. Liu, L. Yang, Y. Liu, D. Sheng, R. Xu, Y. Ge, X. Tu, H. Gao, C. Zhao, *Adv. Electron. Mater.* **2022**, *8*, 2101260.
[43] S. Jafarpour, H. Naghshara, B. Aslibeiki, *Ceram. Int.* **2024**, *50*, 5665.
[44] J. F. Pierdoná Antoniolli, G. L. Grespan, D. Rodrigues Jr, *ChemSusChem* **2024**, *17*, 202301808.
[45] F. Liu, L. You, K. L. Seyler, X. Li, P. Yu, J. Lin, X. Wang, J. Zhou, H. Wang, H. He, *Nat. Commun.* **2016**, *7*, 12357.
[46] L. W. Martin, A. M. Rappe, *Nat. Rev. Mater.* **2016**, *2*, 16087.
[47] Z. Wu, C. Ji, L. Li, J. Kong, Z. Sun, S. Zhao, S. Wang, M. Hong, J. Luo, *Angew. Chem., Int. Ed.* **2018**, *57*, 8140.
[48] X. Wu, S. Chen, M. Moser, A. Moudgil, S. Griggs, A. Marks, T. Li, I. McCulloch, W. L. Leong, *Adv. Funct. Mater.* **2023**, *33*, 2209354.
[49] J. Hafner, *J. Comput. Chem.* **2008**, *29*, 2044.
[50] J. P. Perdew, K. Burke, M. Ernzerhof, *Phys. Rev. Lett.* **1996**, *77*, 3865.
[51] G. I. Csonka, J. P. Perdew, A. Ruzsinszky, P. H. T. Philipsen, S. Lebègue, J. Paier, O. A. Vydrov, J. G. Ángyán, *Phys. Rev. B* **2009**, *79*, 155107.